**Supplementary Materials for L2-CPI: High-Resolution Computational Phase Imaging with an Infinite Field of View**

Supplementary 1: Image acquisition and phase retrieval.
Figure S1: The process of retrieving the phase profile from interferograms.
Supplementary 2: Comparison between the four-parameter cosine fitting algorithm and the fast three-parameter cosine fitting algorithm.
Figure S2: Comparison of the four-parameter cosine fitting algorithm with the fast three-parameter cosine fitting algorithm in speed.
Supplementary 3: Derivation of the fast three-parameter cosine fitting algorithm.
Supplementary 4: Derivation of the conventional 7-step phase-shifting algorithm with an estimated phase-shifting value.
Supplementary 5: Design and SEM Characterization of an IDA Wafer with Defects
Figure S3: Design layout and SEM images of the IDA samples.
Supplementary 6: Specifications for transparent samples and their ideal surface profile
Supplementary 7: Numerical simulation of the bx-bridge defect signal
Figure S4: Numerical simulation results of the bx-bridge defect and the relationship between the PV value of the bx-bridge defect signal and the defect size
Supplementary 8: Physical factors affecting defect signals
Figure S5: The influence of the focal plane and polarization direction on the phase signal intensity of the bx-bridge defect on the IDA wafer sample.
Supplementary 9: Analysis of image stitching in digital holography
Figure S6: Schematic diagram of the disadvantages of image stitching.
Supplementary 10: The difference in time and travel between stitching and continuous scanning
Figure S7: Comparison of velocity and travel between stitching and continuous scanning.

**SUPPLEMENTARY 1: IMAGE ACQUISITION AND PHASE RETRIEVAL**

The complete acquisition process of the sampling sequence is illustrated in Fig. S1a. The scanning direction is along the *x*-axis, and the orientation of the interference fringes' intensity variation is parallel to the scanning direction, as shown in Fig. S1a. A specific area on the sample will enter from one side of the camera and leave from the other as the sample stage moves. To ensure that there are as many fitting points as possible (to achieve an excellent fitting result while avoiding the waste of computational resources caused by overlap sampling), the scanning speed $v$ of the stage is required to be precisely matched with the frame rate $f$ of the camera, *i.e.*,

$$v = \frac{w \times f}{M} \tag{S1}$$

where $M$ is the magnification factor, and $w$ is the width of a pixel of the camera. This scanning speed ensures pixel-level movement, *i.e.*, the images of the sample captured by the camera move by only one column of pixels at a time. As a result, the sample experiences a complete phase shift during the scanning process as the sample moves, as shown in Fig. 1c. To detail the principle of phase retrieval for the sample, an arbitrarily given cross-section on the sample's surface is presented as an example in Fig. S1a α, labeled as the interferogram line in the red box. The interferogram lines with complete phase shifts are extracted and arranged in the order of scanning to obtain the sampling sequence, as shown in Fig. S1a β. After that, the phase profile of the cross-section on the sample's surface can be obtained by retrieving the phase from this sampling sequence using a phase retrieval algorithm, and the retrieved phase profile of the cross-section is shown in Fig. S1a γ.

The phase map is generated by stacking the phase profile retrieved from sampling sequences produced during the scanning process. As the scanning progresses, each cross-section on the sample's surface generates a corresponding sampling sequence, ultimately leading to the phase distribution of the entire sample. In Fig. S1b, the sample image enters the sensor from column *a* and exits the sensor from column *d*. A complete sampling sequence is achieved if the designated area exists in the sensing area of the camera sensor (*i.e.*, enter from column a, exit from column d), as shown in Fig. S1b. Only if the velocity of the sample stage in Eq. S1 is uniform; the phase profile can be collected and calculated accurately.

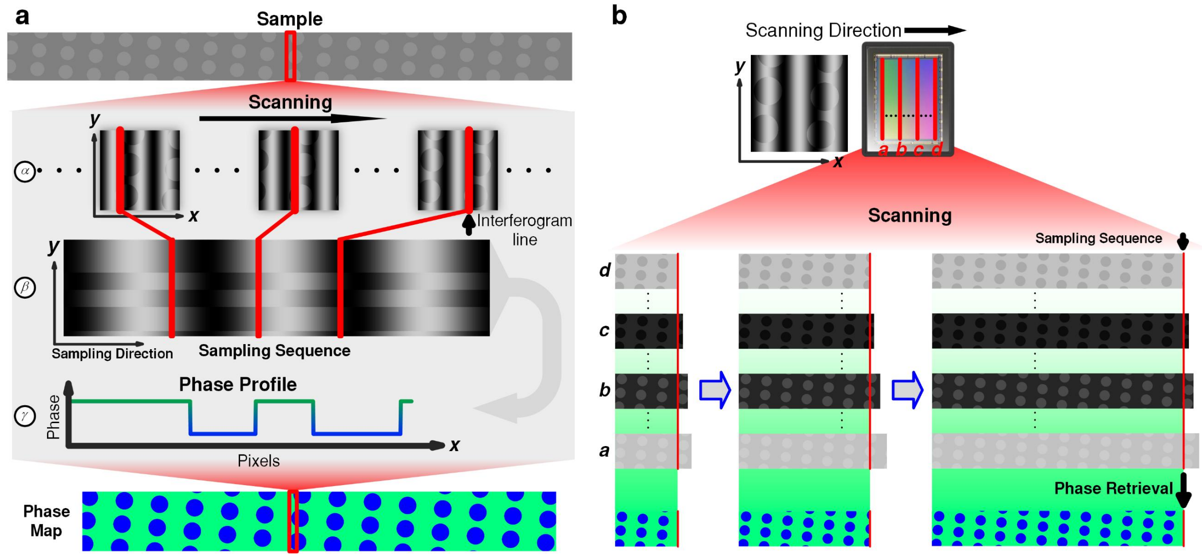


**Figure S1 a,** The process of retrieving the phase profile from interferograms. The red box on the sample represents the selected measurement area, which corresponds to the area marked by the red box in the phase map. **b,** The process of scanning to generate a phase map. The red a and d corresponding to the red lines represent the pixel columns at the camera's far left and far right, respectively. The red b and c corresponding to the red lines represent any two-pixel columns on the camera. The black letters a, b, c, and d represent all images collected by the pixel columns a, b, c, and d at different time points during the scanning process.

## SUPPLEMENTARY 2: COMPARISON BETWEEN THE FOUR-PARAMETER COSINE FITTING ALGORITHM AND THE FAST THREE-PARAMETER COSINE FITTING ALGORITHM

The fast three-parameter cosine fitting algorithm has a faster running speed than the four-parameter cosine fitting algorithm. This is because the four-parameter cosine fitting algorithm involves a nonlinear iterative process during the fitting, significantly slowing down its execution speed. In contrast, the fast three-parameter cosine fitting algorithm consists entirely of linear operations, significantly alleviating the computational burden. In Fig. S2, we compare the consuming time required by both algorithms after 1,700 runs, where the fast three-parameter cosine fitting algorithm is hundreds of times faster than the four-parameter cosine fitting algorithm.

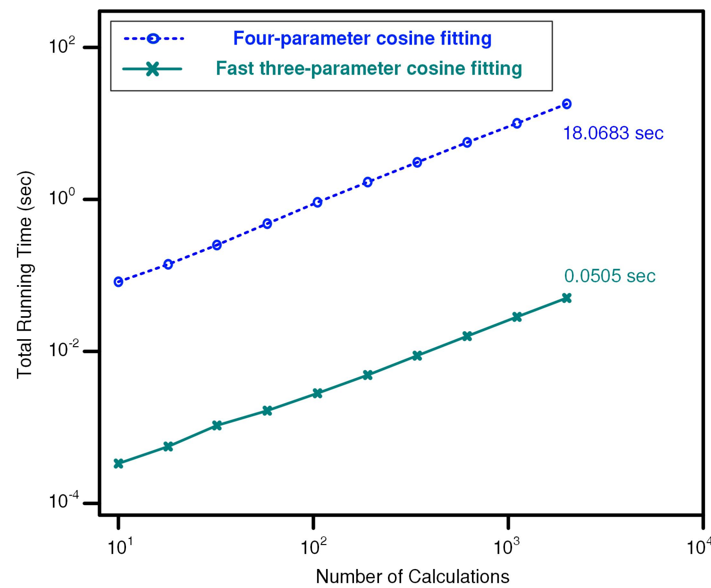


**Figure S2** Comparison of the four-parameter cosine fitting algorithm with the fast three-parameter cosine fitting algorithm in terms of speed.

**SUPPLEMENTARY 3: DERIVATION OF THE FAST THREE-PARAMETER COSINE FITTING ALGORITHM**

For more straightforward computation, we have converted the signal $I$ from the standard representation in terms of amplitude and phase to the following form:

$$I(x) = a\cos t\omega + b\sin t\omega + c \tag{S2}$$

Following the transformation, the fitting function can be expressed more discreetly. Compare the above Eq. (S2) with the actual measured signal $I(t)_{measurement}$, and define the sum of squared errors as:

$$f(a,b,c)_{\min} = \sum \varepsilon_i^2 = \sum \left[ I(t)_{measurement} - I(t) \right]^2 \tag{S3}$$

To find the values of $a$, $b$, and $c$ that minimize $f$, take the partial derivatives of $a$, $b$, and $c$ in Eq. (S9) and set them to 0:

$$\begin{cases} \dfrac{\partial f}{\partial a} = 2\sum \cos x\omega \left[ I(t)_{measurement} - I(t) \right] \\ \dfrac{\partial f}{\partial b} = 2\sum \sin x\omega \left[ I(t)_{measurement} - I(t) \right] \\ \dfrac{\partial f}{\partial c} = 2\sum \left[ I(t)_{measurement} - I(t) \right] \end{cases} \tag{S4}$$

After rearranging the formula, we have

$$\begin{cases} a\sum \cos^2 t\omega + b\sum \sin t\omega \cos t\omega + c\sum \cos t\omega = \sum I(t)\cos t\omega \\ a\sum \sin^2 t\omega + b\sum \sin t\omega \cos t\omega + c\sum \sin t\omega = \sum I(t)\sin t\omega \\ a\sum \cos t\omega + b\sum \sin t\omega + c\sum 1 = \sum I(t) \end{cases} \tag{S5}$$

By solving the system of linear equations, we can obtain the values of $a$, $b$, and $c$, *i.e.*,

$$\begin{bmatrix} a \\ b \\ c \end{bmatrix} = \begin{bmatrix} \sum \cos^2 t\omega & \sum \sin t\omega \cos t\omega & \sum \cos t\omega \\ \sum \sin t\omega \cos t\omega & \sum \sin^2 t\omega & \sum \sin t\omega \\ \sum \cos t\omega & \sum \sin t\omega & \sum 1 \end{bmatrix}^{-1} \begin{bmatrix} \sum I(t)\cos t\omega \\ \sum I(t)\sin t\omega \\ \sum I(t) \end{bmatrix} \tag{S6}$$

Since the system of linear equations is consistent, there is only one solution, so the obtained values of $a$, $b$, and $c$ are the best-fitting results. When the fitting is performed with data having a length that is a multiple of the period, the result will be significantly simplified, *i.e.*,

$$\begin{bmatrix} a \\ b \\ c \end{bmatrix} = \begin{bmatrix} -2\sum I(t)\sin t\omega / n \\ 2\sum I(t)\cos t\omega / n \\ \sum I(t) / n \end{bmatrix} \tag{S7}$$

After obtaining $a$ and $b$, the phase value $\phi$ of the sample can be easily obtained through

$$\phi = \arctan\frac{b}{a} = \arctan\frac{-2\sum I(t)\sin(t\omega)}{2\sum I(t)\cos(t\omega)} \tag{S8}$$

## SUPPLEMENTARY 4: DERIVATION OF THE CONVENTIONAL 7-STEP PHASE-SHIFTING ALGORITHM WITH AN ESTIMATED PHASE-SHIFTING VALUE

We compare the conventional 7-step phase-shifting algorithm with the fast three-parameter cosine fitting algorithm. The 7-step phase shift algorithm can be derived from trigonometric transformations. By selecting 7 columns of interferogram lines evenly in the sampling sequence, we can obtain the following 7 equations:

$$\begin{aligned} I_1 &= A + B\cos(\phi + 3\Delta) \\ I_2 &= A + B\cos(\phi + 2\Delta) \\ I_3 &= A + B\cos(\phi + \Delta) \\ I_4 &= A + B\cos(\phi) \\ I_5 &= A + B\cos(\phi - \Delta) \\ I_6 &= A + B\cos(\phi - 2\Delta) \\ I_7 &= A + B\cos(\phi - 3\Delta) \end{aligned} \tag{S9}$$

where $\Delta$ is the phase-shift value between two interferogram lines. By combining similar terms in Eq. (S2), we have

$$\begin{aligned} I_1 - I_7 &= -2B\sin\phi\sin 3\Delta \\ I_3 - I_5 &= -2B\sin\phi\sin\Delta \\ I_2 + I_6 &= 2A + 2B\cos\phi\cos 2\Delta \\ I_4 &= A + B\cos\phi \end{aligned} \tag{S10}$$

To obtain tan $\phi$, we eliminate the background light intensity $A$ by taking the difference and separately extracting the sin $\phi$ and cos $\phi$ terms:

$$\begin{aligned} -(I_1 - I_7) + 7(I_3 - I_5) &= B\left(-8\sin\Delta - 8\sin^3\Delta\right)\sin\phi \\ -4(I_4 + I_6) + 8I_4 &= B\left(16\sin^2\Delta\right)\cos\phi \end{aligned} \tag{S11}$$

Finally, tan $\phi$ can be represented as

$$\frac{-(I_1 - I_7) + 7(I_3 - I_5)}{-4(I_4 + I_6) + 8I_4} = \frac{-1 - \sin^2\Delta}{2\sin\Delta} \bullet \tan\phi \tag{S12}$$

The intensity at each point in the interferogram changes with the variation of the phase shift $\alpha$. Due to the equidistant gap between the selected columns of pixels on the camera, the phase shift between two adjacent interferograms remains constant. Usually, the phase shift in phase-shifting interferometry is fixed at $\pi/4$. However, the absolute phase-shifting values cannot be directly determined if the tilting angle of the reference mirror cannot be accurately measured. $L^2$-CPI cannot guarantee the precise phase-shifting values. Fortunately, the phase shift can be roughly estimated as

$$\Delta = \arctan\sqrt{\left[\frac{3(I_3 - I_5) - (I_1 - I_7)}{(I_1 - I_7) + (I_3 - I_5)}\right]} \tag{S13}$$

here $\Delta$ represents the phase shift at each point on the phase-shift images. Now, with the known phase shift, it

is easy to obtain the phase distribution through simple trigonometric transformations, *i.e.*,

$$\phi = \arctan\left[\frac{2\sin\alpha}{-1-\sin^2\alpha}\bullet\frac{-(I_1-I_7)+7(I_3-I_5)}{-4(I_2+I_6)+8I_4}\right] \tag{S14}$$

## SUPPLEMENTARY 5: DESIGN AND SEM CHARACTERIZATION OF AN IDA WAFER WITH DEFECTS

The design layout of a single cell in the IDA wafer sample is shown in Fig. S3a. The critical dimension (CD) of this cell is 60 nm, and it contains two nanowires. The dimensions of all elements within a single cell are labeled in Fig. S3a. The scanning electron microscope image of the fabricated IDA wafer is shown in Fig. S3b. We present two types of defects found in the smallest fabricated structure, with a CD of 60 nm, as shown in Fig. S3. Defects of each type are fabricated within a large block and arranged in a left-center-right distribution across the block. The figure magnifies and displays three types of defects located in the left, center, and right regions, with their dimensions clearly labeled. The defect size of a Bx-bridge is defined as the width of the bridging structure, while the defect size of a cutting defect is defined as the length of the break. Notably, the defect sizes increase progressively from left to center and then to right. In the experiments described in the manuscript, we utilized the defect pattern located in the central region. In the experiments detailed in Supplementary 7, the defect pattern was positioned in the right region. In the experiments described in the "Patterned Wafer Defect Inspection" subsection of the Results chapter, the defect pattern was located in the center region.

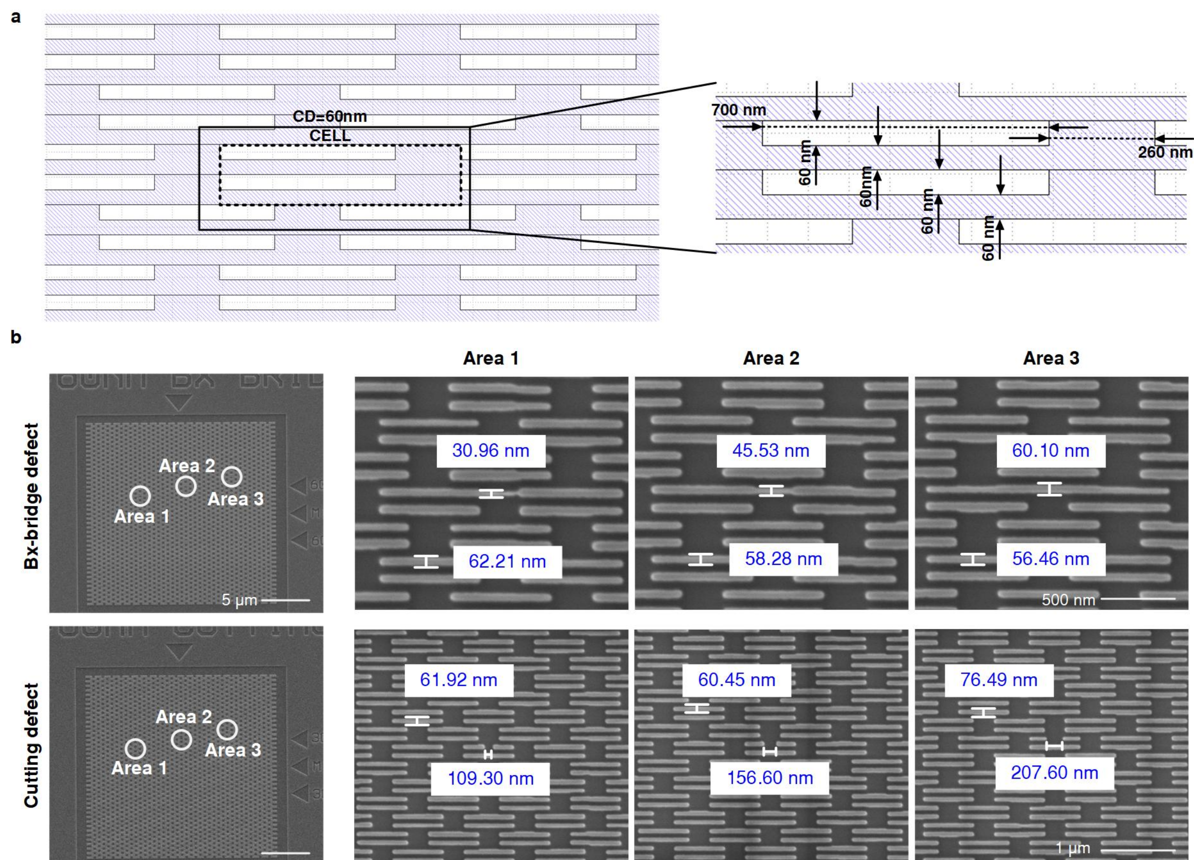


**Figure S3 a,** The design of an IDA sample cell with a CD of 60 nm, where the black dashed box within the black square represents one cell. It consists of two nanowires, each with a linewidth of 60 nm, and their dimensions are annotated on the right. **b,** SEM images of the IDA samples (Nova NanoSEM 450).

## SUPPLEMENTARY 6: SPECIFICATIONS FOR TRANSPARENT SAMPLES AND THEIR IDEAL SURFACE PROFILE

The transparent microlens array (MLAS10-F05-P150-AB, LBTEK Inc.) is composed of microlenses arranged in a two-dimensional grid on a UV-fused silica substrate. The array thickness is 1.2 mm, the array pitch is 150 μm, the microlens diameter is 143 μm, and the microlens focal length is 5.2 mm. One side of the microlens is flat, while the other side is etched with a microspherical array structure. According to the thin lens formula, the radius of curvature of the microlens spherical surface can be calculated:

$$\frac{1}{f}=(n-1)\left(\frac{1}{R_1}-\frac{1}{R_2}\right) \tag{S15}$$

where $f$ is the focal length of the microlens, $n$ is the refractive index of the material, which is set to 1.4607 at 532 nm here. Specifically, $R_2$, the radius of curvature of the flat surface, is infinitely large, while $R_1$, the radius of curvature of the microlens, is calculated to be $R_1$ = 2395.64 μm.

The phase calibration slide (Phasics Inc.) is a piece of etched silica that introduces stable and known phase shifts. The serial number is 2004. It is designed to work with standard microscope magnifications. The depth of its etched holes is defined in the calibration report by the optical path difference (OPD):

$$OPD=e_1\times(n_2-n_1) \tag{S16}$$

where $e_1$ is the etching depth, and $n_2$ and $n_1$ are the refractive indices of silica and the surrounding environment, respectively. Samples labeled N and O are biological replicas. We selected pattern O, which is composed of dispersed clones of the same binary bacteria, grouped in 3 different scales. From this, we chose the largest scale, with a nominal average OPD of 88.5 nm and a standard deviation of 12.8 nm. The measurement light source had a wavelength of 625 nm, and at this point, the refractive index of silica was 1.4572. Based on eq. (5) and eq. (S16), the etching depth was calculated to be 215.62 nm, with a standard deviation of 28.0 nm.

## SUPPLEMENTARY 7: NUMERICAL SIMULATION OF THE BX-BRIDGE DEFECT SIGNAL

We use the bx-bridge as an example to perform a simulation analysis of the defect phase signal. Specifically, we simulate the smallest critical dimension (CD) pattern that can be successfully fabricated, *i.e.*, with a CD of 60 nm. First, we model the structure, which consists of a base geometry of nanowires with dimensions of 60 nm in width, 700 nm in length, and 60 nm in height. These nanowires are paired and filled within cells measuring 240 nm in width and 960 nm in length, uniformly distributed in a staggered arrangement across the entire simulation domain. In Ansys Lumerical, the sample structure is illuminated with a plane wave at a wavelength of 532 nm, and the near-field complex amplitude of the reflected light is captured. Subsequently, a vector diffraction imaging algorithm is employed to compute the far-field phase distribution under a numerical aperture (NA) of 0.8. We simulate both defective and non-defective structures with a defect size of 60 nm, as shown in Fig. S4a, and calculate the differential image by subtracting the two.

To investigate the relationship between defect size and defect signal intensity, we also simulated various defect sizes. Under the same structural configuration, we applied different defect sizes and plotted the P-V values of the differential signals as a curve, as shown in Fig. S4b. It can be observed that the bx-bridge defect maintains a relatively strong signal at a defect size of 25 nm, but experiences a sharp decline when the defect size is reduced to 20 nm. At a defect size of 10 nm, the signal intensity is only one-fourth of that at a defect size of 35 nm. At this point, the defect signal P-V value is approximately 0.1 rad. In practical measurements, noise makes it difficult to distinguish the defect signal.

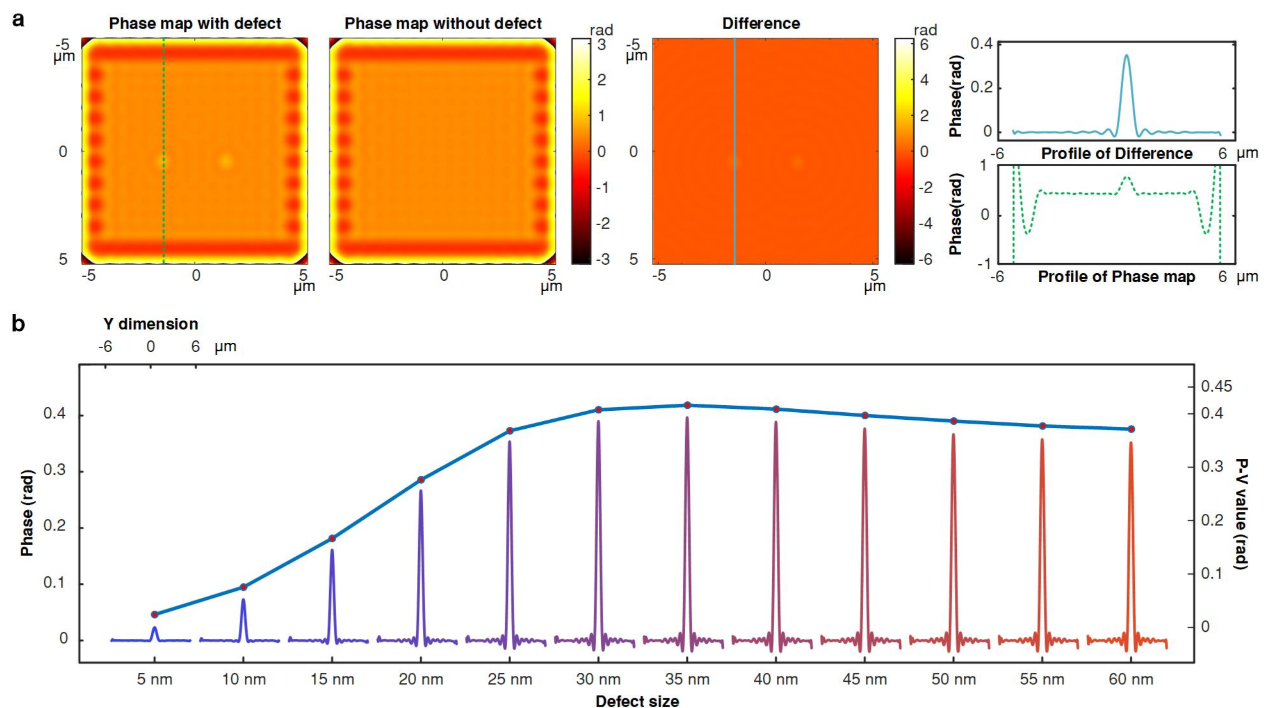


**Figure S4 a,** Numerical simulation results of the bx-bridge defect structure, with an IDA critical dimension of 60 nm and a defect size of 60 nm. The Difference graph illustrates the differential mapping between the

phase map containing defects and the phase map devoid of defects. The blue solid profile line represents the defect location profile in the difference graph, while the green dashed profile line corresponds to the defect location profile in the phase map with defects. **b,** The relationship between the PV value of the bx-bridge defect signal and the defect size, with an IDA critical dimension of 60 nm. The left vertical axis corresponds to the differential signal profile lines for varying defect sizes, while the right vertical axis corresponds to the blue polyline.

## SUPPLEMENTARY 8: PHYSICAL FACTORS AFFECTING DEFECT SIGNALS

To investigate the physical factors affecting the defect phase, we prepared two sets of experiments to separately study the influence of the focal plane position and the polarization angle on the disturbance of the defect phase. We selected the phase measurement results of the bx-bridge defect with a CD of 60 nm and a defect size of 60 nm as the evaluation criterion. As shown in Fig. S5a, we used VS-PSI as the benchmark for our experiments because it has been verified in the manuscript that our $L^2$-CPI has almost identical phase accuracy to VS-PSI. Although VS-PSI exhibits more significant noise, it does not affect our summary of the phase variation patterns. We control the z-axis displacement stage, which carries the sample, to scan across the focal plane. The measurement results are presented in Fig. S5b. The phase signal intensity initially increases and subsequently decreases as the process of defocusing, refocusing, and defocusing again takes place. The signal most closely matches the simulated value at the "In focus" position. This confirms that the phase signal intensity at the bx-bridge defect is strongly dependent on the focal plane position, reaching its maximum defect phase signal strength when the focal plane is in focus. We utilize the half-wave plate depicted in Fig. 1c to adjust the polarization angle of the incident light, investigating the effect of illumination with varying polarization angles on the phase signal intensity of defects. The horizontal direction of the image is defined as the 0° polarization angle, where the polarization direction of the light is nearly parallel to the long axis of the nanowires in the IDA. Subsequently, we rotate the half-wave plate clockwise in 5° increments, corresponding to a 10° increase in the polarization angle, and conduct measurements incrementally. The results of these measurements are presented in Fig. 5c. Due to a slight clockwise rotation of our sample relative to the horizontal axis, the maximum phase signal intensity occurs not at the 0° polarization angle, but instead at 10°. As the polarization angle increases further, the defect phase signal gradually diminishes. Thus, we conclude that the phase intensity of the bx-bridge defect is highly sensitive to the polarization direction of the incident light, with the optimal polarization orientation being parallel to the long axis of the nanowires.

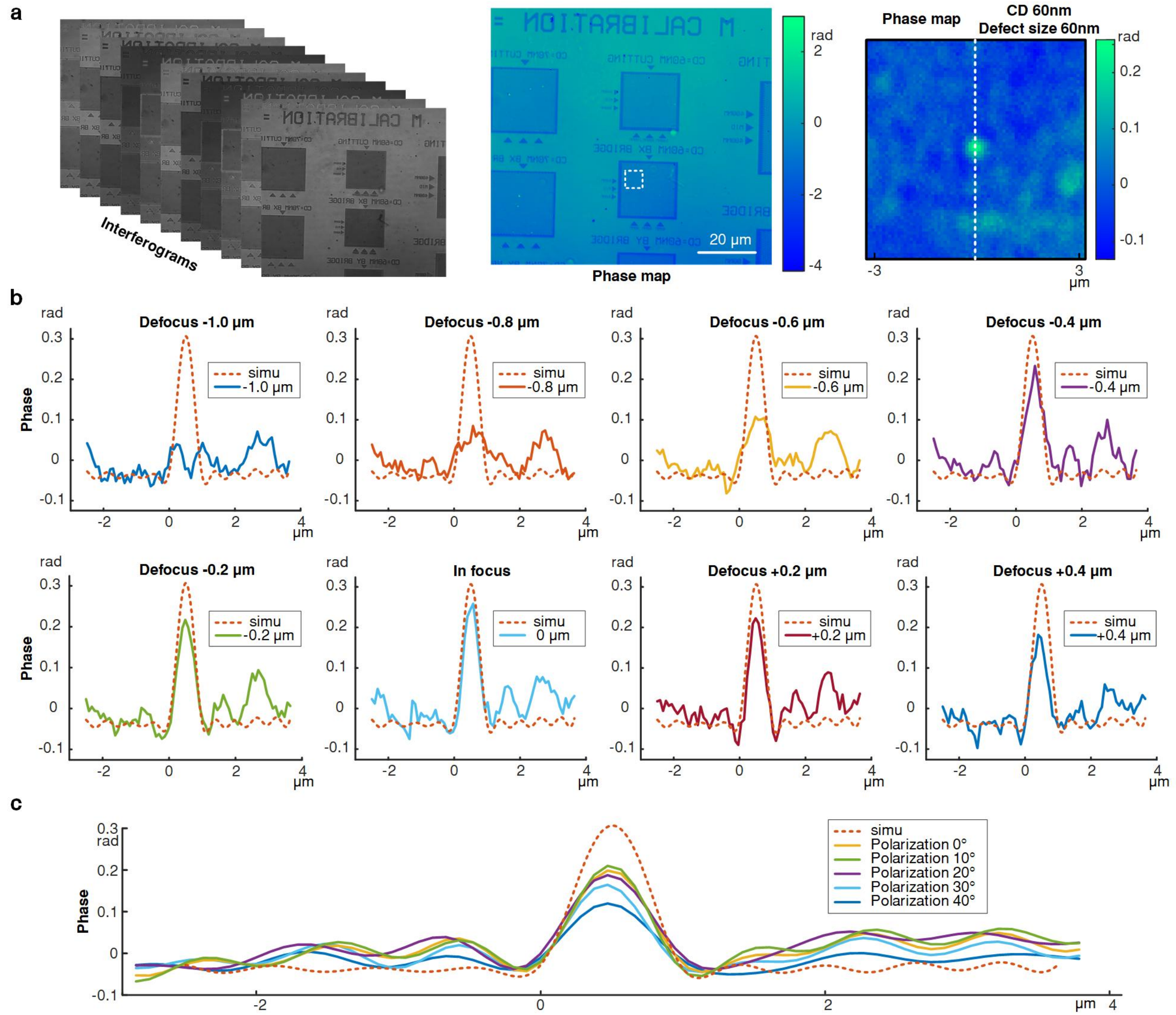


**Figure S5 a,** The test results for the bx-bridge defect using VS-PSI, with an IDA critical dimension of 60 nm and a defect size of 60 nm, are presented. Due to the left-right mirroring of the image, the test area corresponds to Area 3 in Fig. S3. **b,** Comparison of signal intensity of the bx-bridge defect at different focal planes with the simulated values in Supplementary 7. In each measurement, the focal plane steps by 200 nm, ranging from -1.0 μm to +0.4 μm. **c,** Comparison of the signal intensity of the bx-bridge defect under different illumination polarization angles with the simulated values in Supplementary 7. The polarization angle of 0° corresponds to the horizontal direction, and the polarization angle varies clockwise from 0° to 40°.

## SUPPLEMENTARY 9: ANALYSIS OF IMAGE STITCHING IN DIGITAL HOLOGRAPHY

Conventional Quantitative Phase Imaging (QPI) methods, such as Digital Holographic Microscopy (DHM), are constrained by a fixed field of view in single-shot imaging. To achieve large-area imaging, image stitching is required to ensure complete coverage. This process introduces two primary challenges, as illustrated in Fig. S6a: the overlap between adjacent images and the alignment of interference fringes or reference phases, collectively referred to as "near error", which characterizes discrepancies between neighboring images. Image overlap arises because adjacent images must share common regions during the stitching process to enable accurate registration. Image misalignment occurs when there is an offset between the reference plane and the focal plane during scanning in QPI. This offset induces a shift in the reference phase plane, leading to artifacts associated with phase misalignment. These challenges impact the final imaging outcomes, necessitating overlap registration and phase misalignment artifacts, as illustrated in Fig. S6b.

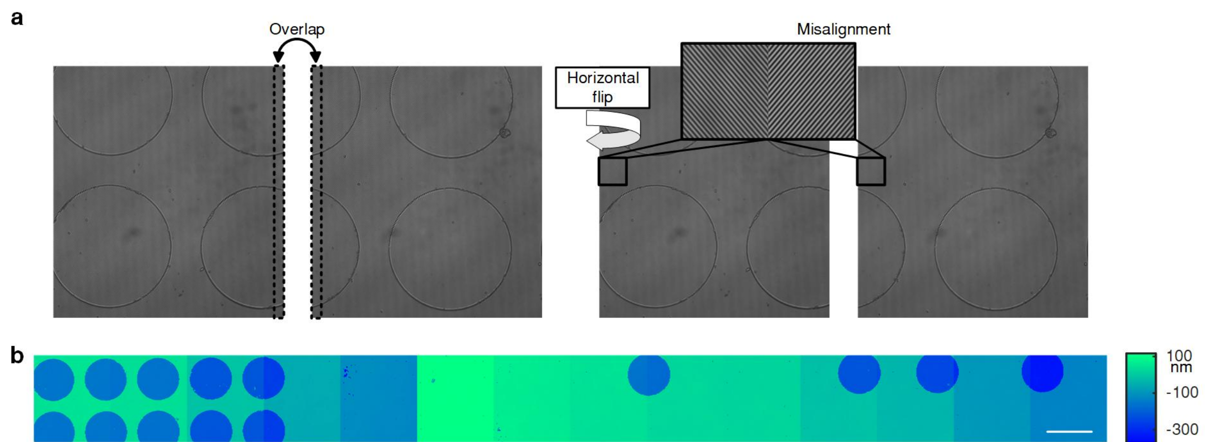


**Figure S6 a,** Two familiar sources of error in image stitching. **b,** Schematic diagram of the image directly stitched by DHM without calibration processing. Scale bar: 50 μm.

## SUPPLEMENTARY 10: THE DIFFERENCE IN TIME AND TRAVEL BETWEEN STITCHING AND CONTINUOUS SCANNING

Taking the sample areas measured in Fig. 3c and Fig. S6b as examples, we compare the measurement time and travel of the traditional stitching measurement method with the continuous measurement method of $L^2$-CPI at the same scanning speed. The measurement speed is set to 40 µm/s, and the acceleration is 400 µm/s². Scanning the area depicted in Fig. 3c entails a scanning distance of 1317.1 µm, while the total imaging length in Fig. S6b is 1372.9 µm, with a required scanning distance of 1274.9 µm. As illustrated in Fig. S7a and b, the continuous measurement method enables uninterrupted scanning, completing the process in 32.93 seconds. In contrast, the stitching measurement method involves frequent start-stop operations, necessitating additional time for the displacement stage to stabilize. Assuming a combined stabilization and image acquisition time of 0.5 seconds per operation, the total time required is 39.67 seconds. By eliminating the need for repeated stopping and restarting, the continuous measurement method significantly saves time. As the scanning range expands and scanning speed increases, the temporal advantage of the continuous measurement method becomes increasingly pronounced.

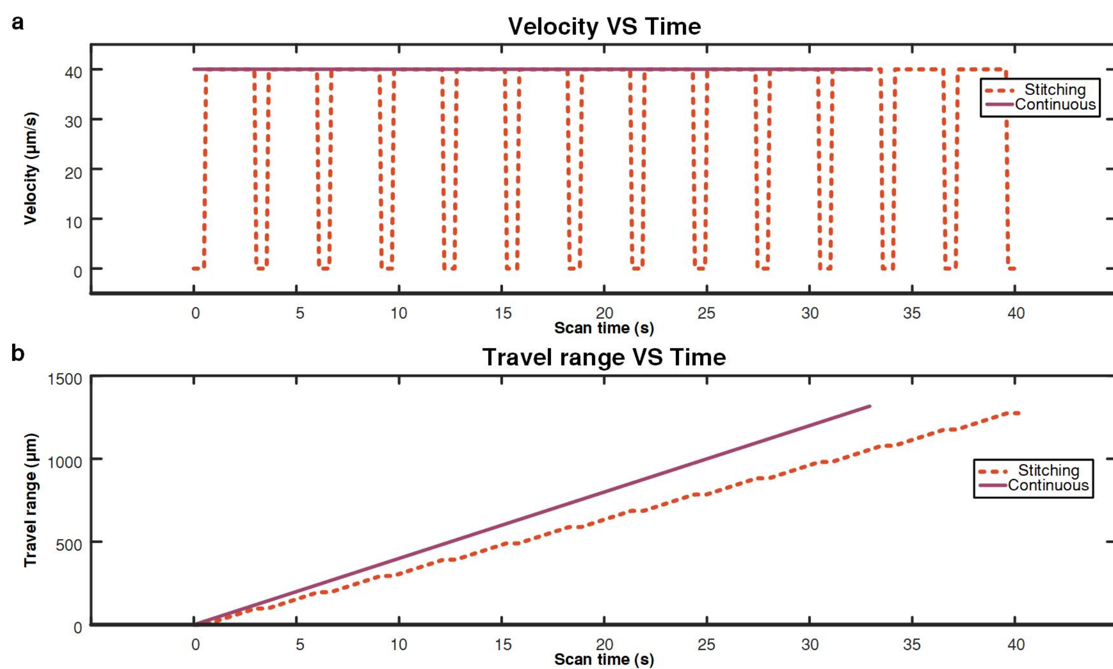


**Figure S7 a,** The relationship diagram of speed and time between stitching measurement and continuous scanning measurement. **b,** The relationship diagram of travel and time between stitching measurement and continuous scanning measurement. The total travel range of continuous measurement is 1317.1 µm, while the total travel range of stitching measurement is 1274.9 µm.